RSC Advances

PAPER

View Article Online
View Journal | View Issue

Cite this: *RSC Adv.*, 2017, **7**, 6835

Self-assembled Co_9S_8/RGO-CNT interconnected architecture as composite electrode for supercapacitors†

Wen Chen, Ye Li, Xiao Han, Xiaoran Zhao and Yan Zhao*

Received 5th December 2016
Accepted 31st December 2016

DOI: 10.1039/c6ra27685g

www.rsc.org/advances

Co_9S_8 nanoparticles are dispersed homogeneously on the backbone of self-assembled RGO-CNT by using hydrothermal and vacuum filtration method. The interconnected structure of Co_9S_8/RGO-CNT generates a profound impact on the electrode, resulting from the addition of CNTs into RGO/Co_9S_8, forming a 3D intertwined structure. The composite electrode shows a high specific capacitance of 1376.78 F g^{-1}, which is much higher than that of graphene or Co_9S_8 as electrode material, and excellent cycling stability at the scan rate of 5 mV s^{-1}. In addition, the composite electrode exhibits brilliant long-term stability with the specific capacitance of 894.9 F g^{-1} after 500 charge/discharge cycles. The Co_9S_8/RGO-CNT composite with interconnected architecture is a promising electrode candidate for supercapacitors.

1 Introduction

Supercapacitors have been widely researched because of their increasing applications not only in computers, cameras and other small power devices, but also in the trigger devices of automobiles and large wind power plants.[1–3] Supercapacitors have higher power density, faster charge–discharge ability, longer life cycle and higher efficiency compared with traditional batteries.[4–7] However, the energy density of supercapacitors is low, which can restrict their applications. It is reported that high energy density can be achieved by pseudocapacitive reactions, such as those using RuO_2, MnO_2, Co_3O_4, V_2O_5, NiO, *etc.*[8–12] In addition, metal sulfide-based supercapacitors of the same element group have also been studied.[3] Wang and coworkers showed that the CoS_2-based supercapacitor electrode achieved 314 F g^{-1} at the current density of 0.5 A g^{-1}.[3] Similarly, Ranga Rao synthesized hierarchical structured Co_3O_4 with high porosity, and charge–discharge measurement results indicated that this electrode material can attain 548 F g^{-1} at the current density of 8 A g^{-1}.[10] However, such specific capacitances are still relatively low in the application of electrical devices. Thus, it is essential to hybridize supercapacitors with pseudocapacitive materials to achieve high specific capacitance and high energy density.

Graphene has been regarded as a promising electrode material for supercapacitor application because of its ultrathin surface area and excellent electrical conductivity.[13–16] However, monolayer graphene units often stack into multilayers, which can cause a great loss to surface area of graphene. Thus, graphene supercapacitors have low capacitance caused by the stacking of graphene. It is worth noting that metal oxide or sulfide nanoparticles, such as Co_3O_4/RGO, MnO_2/GNS, and CoS_2/RGO, may be used as spacers to prevent graphene monolayers from stacking.[3,9,10] In addition, inserting some conductive carbons materials, such as carbon nanotubes (CNT), between graphene sheets can link graphene sheets into a stable network, which can effectively prevent the stacking of graphene sheets.[17,18] Niu and coworkers synthesized the graphene/CNT interconnected network for lithium sulfur batteries with an initial capacity of 1008 mA h g^{-1} at 0.3C and capacity retention of 70% after 100 cycles.[17] Many recent research studies reported that cobalt sulfide exhibits great performance as an electrode material for supercapacitors, which results from its various nanostructures.[19,20]

Herein, we report Co_9S_8 with graphene and CNT-based materials. On the one hand, the large specific surface of graphene can benefit the loading of Co_9S_8 nanoparticles;[21] on the other hand, CNTs link the graphene sheets and form a intertwined, connected structure, which can make more paths for electrons and ions.

2 Experimental

2.1 Materials

Natural flake graphite and cobaltous sulfate heptahydrate ($CoSO_4 \cdot 7H_2O$) were purchased from GuoYao Group Chemical Reagent Co., Ltd, China. Multiwalled carbon nanotubes (MWCNTs) were purchased from Beijing TianNai Co., Ltd, China. Sulphuric acid, potassium permanganate, hydrogen peroxide, thiourea, potassium nitrate, ammonia and glucose were purchased from Beijing Chemical Factory; all these reagents were of analytical grade.

Beihang University, China. E-mail: jennyzhaoyan@buaa.edu.cn

† Electronic supplementary information (ESI) available. See DOI: 10.1039/c6ra27685g

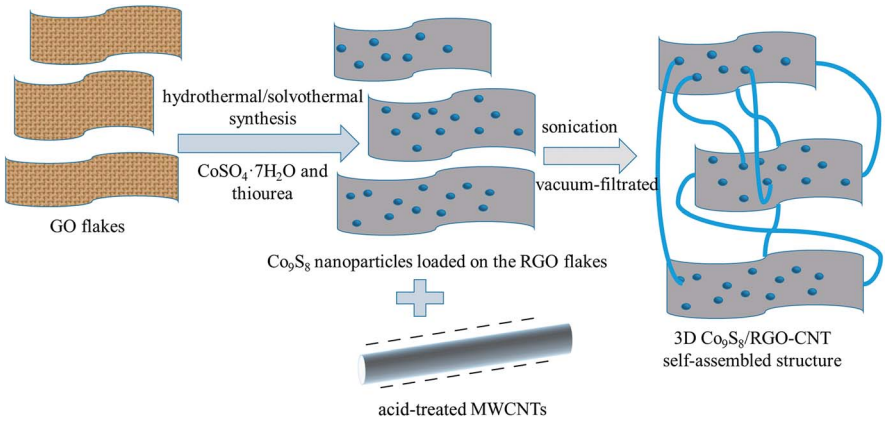

Fig. 1 Scheme of preparation of Co_9S_8/RGO-CNT.

2.2 Synthesis of Co_9S_8/RGO-CNT composites

GO was prepared by modified Hummers' method, and MWCNTs were acid-treated with concentrated H_2SO_4 (60 mL) and KNO_3 (1.5 g) at 70 °C for 7 h.[22–25] As for Co_9S_8/RGO-CNT composite synthesis, about 1.2 g $CoSO_4 \cdot 7H_2O$ was dissolved in 30 mL of ethylene glycol (EG) and 10 mL of deionized water under stirring, then about 0.6 g thiourea was dispersed into this scarlet-red solution. About 65 mg of GO was dissolved in the aforementioned scarlet-red solution through sonication for 1 h. Then, 2 mL ammonia and 0.1 g glucose were added into the mixed solution, which was then transferred into a 50 mL Teflon-lined stainless-steel autoclave and heated in an oven at 170 °C for 10 h. After cooling to room temperature naturally, Co_9S_8/RGO powder was finally obtained by centrifugation, washing thoroughly with DI water and ethanol repeatedly, and drying at 60 °C for 7 h in a vacuum oven. Next, CNTs were added into the Co_9S_8/RGO aqueous solution through vacuum filtration and sonication. For self-assembly of the Co_9S_8/RGO-CNT composite, Co_9S_8/RGO and surface-modified CNTs (Co_9S_8/RGO : CNTs = 3 : 1 wt ratio) were dispersed evenly with the addition of 3 mg CTAB in 100 mL of DI water under sonication for 2 h. Then, the solution was vacuum-filtrated with a polytetrafluoroethylene (PTFE) membrane, pore size = 0.2 μm, and self-assembled Co_9S_8/RGO-CNT film was formed during the filtration process and designated as 30% CNT. Two other Co_9S_8/RGO-CNT composites were prepared by changing the amount of CNTs (10 wt% and 50 wt%), and the samples were designated as 10% CNT and 50% CNT, respectively. For comparison, pure Co_9S_8/RGO was also prepared following the same procedure in the absence of CNTs.

2.3 Characterization

The physical properties of the Co_9S_8/RGO-CNT were examined with X-ray diffraction (XRD), cold cathode analytical field emission scanning electron microscopy (FESEM), transmission electron microscopy (TEM) and X-ray photo-electron spectroscopy (XPS).

XRD analysis was obtained with a Rigaku D/max-2200 with Cu Kα radiation as X-ray source. The SEM images were taken *via* a JSM-7500F for morphological analysis. TEM images were obtained xEI Tecnai G^2 F20 microscope. The chemical state and composition of the composites were measured by XPS *via* an ESCALab 220i-XL spectrometer with a monochromated Al K radiation (1486.6 eV).

2.4 Electrochemical measurements

The electrochemical performance of the Co_9S_8/RGO-CNT electrode was analyzed in a three-electrode cell including a Pt wire as the counter electrode, saturated calomel electrode (SCE) as the reference electrode, a 1 M KOH aqueous solution as the electrolyte and the Co_9S_8/RGO-CNT film loaded on Ni foam (1.0 cm × 1.0 cm) directly as the working electrode.

Herein, cyclic voltammetry (CV) experiments, electrochemical impedance spectroscopy (EIS) and galvanostatic charge–discharge curves were performed using a CHI 660E electrochemical workstation. CV measurements were conducted at a scan rate of 10 mV s^{-1} with the voltage range of −0.1 V to 0.6 V. EIS tests were performed at open-circuit potential in the frequency range between 100 kHz and 0.01 Hz under a perturbation amplitude of 5 mV. Galvanostatic charge–discharge analysis was carried out at various current densities with the voltage range of −0.1 V to 0.3 V. All electrochemically characterized data for each composite given in the report were obtained under identical conditions at room temperature.

The specific capacitance (C) of the electrode can be calculated according to the following equation,

$$C = \frac{\int I \mathrm{d}V}{vmV}, \quad (1)$$

where C (F g^{-1}) is the specific capacitance of the electrode based on the mass of the active materials, I (A) is the current, V (V) is the potential during the discharge and charge process, and m (g) is the mass of the active materials (Fig. 1).

3 Results and discussion

3.1 Structural and morphological characterization of Co_9S_8/RGO-CNT

The composition and purity of the obtained Co_9S_8 sample is shown in Fig. 2a–c. All of the diffraction peaks in this pattern

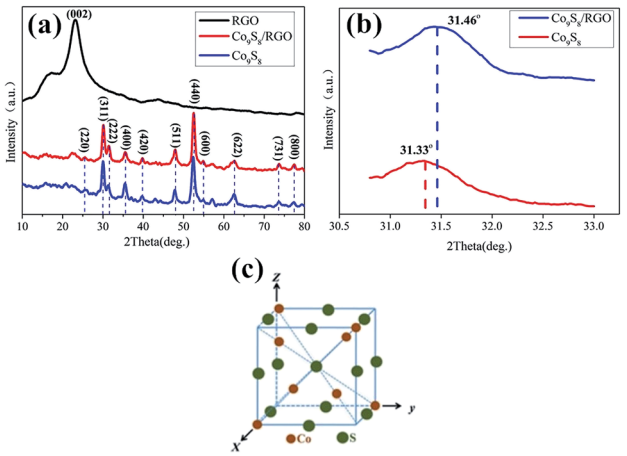

Fig. 2 (a and b) XRD pattern of Co_9S_8 and Co_9S_8/RGO. (c) The crystal structure of Co_9S_8. From (a) and (b), the 2θ of the sample with added graphene is larger than that of the sample without graphene, which confirms the combination of graphene and Co_9S_8 nanoparticles.

can be readily indexed to face-centered cubic Co_9S_8 (JCPDS card no. 65-6801). The crystal structure of Co_9S_8 is shown in Fig. 2c, where the S atoms are arranged through cubic close-packing, 8/9Co atoms are surrounded by a tetrahedron of atoms, and 1/9Co atoms are surrounded by an octahedron of S atoms.[26–28] Comparing the diffraction peaks of the Co_9S_8 and Co_9S_8/RGO samples, there are some differences shown in Fig. 2b; the diffraction peaks of the plane (222) between two samples are different from 2θ and the peak's value, which may be caused by the addition of graphene, and which may prove that there might be some kinds of molecular forces between Co_9S_8 and RGO sheets. The crystal size grown on the surface of the RGO could be calculated by the Scherrer equation:

$$D = \frac{0.89\lambda}{\beta \cos \theta}, \quad (2)$$

where D is crystal dimension, λ is wavelength, β is the full-width-half-maxima of peaks and θ is diffraction angle. According to the Scherrer equation, the crystalline sizes of Co_9S_8 were found to be about 25 nm.

More detailed elemental analysis of the Co_9S_8/RGO sample was done by XPS. Fig. 3a and b shows the core level spectra of the Co 2p and S 2p region. The Co 2p spectrum, including Co $2p_{3/2}$ and Co $2p_{1/2}$, suggest the two spin–orbit doubles characteristic of Co^{2+} and Co^{3+}.[29–31] The S 2p peak at 161.9 eV is the binding energy of Co–S.[32,33] The Co 2p and S 2p peaks in the XPS patterns are characteristic of Co_9S_8.[33]

The microstructures and morphologies of the Co_9S_8/RGO-CNT composite were investigated by SEM. As shown in Fig. 4a, the Co_9S_8 nanoparticles were scattered evenly with a size of about 50 nm on the RGO sheets, and the Co_9S_8 particles are microspheres; it is noteworthy that the particles are uniformly anchored on RGO sheets. The small size and homogenous distribution of Co_9S_8 particles in the Co_9S_8/RGO composite could be attributed to the functional groups on RGO acting as the nucleation sites for Co_9S_8 particles. Fig. 4b–d present SEM images of Co_9S_8/RGO composite with different contents of CNTs. It can been seen easily that Co_9S_8/RGO is well dispersed in the CNT network in Fig. 4c, while in Fig. 4b, part of the Co_9S_8/RGO is out of the CNT network, and in Fig. 4d, lots of CNTs are intertwined together, thus resulting in aggregation. To sum up, it is concluded that proper CNTs added into the Co_9S_8/RGO composite are extremely significant. With Co_9S_8/RGO evenly scattered in the highly conductive CNT network, the 3D hierarchical structure can provide a robust electrical connection within the entire electrode framework, enable the contact with the liquid electrolyte readily, and even maintain such features during the cycling process because of the 3D wrapping effect of the CNTs.[34]

Further microstructures of the Co_9S_8/RGO-CNT composite were characterized by TEM. From Fig. 5a and b, it can be observed that Co_9S_8 particles are well dispersed on the RGO sheets, while aggregation occurred in a portion of the area. Fig. 5c is the high-resolution TEM (HRTEM) image of Co_9S_8/RGO, and it indicates Co_9S_8 particles with a d-spacing of 0.350 nm, 0.299 nm and 0.220 nm, which correspond to the (220), (311) and (420) planes of Co_9S_8, respectively. As for the TEM image of the Co_9S_8/RGO-CNT composite in Fig. 5d, it is

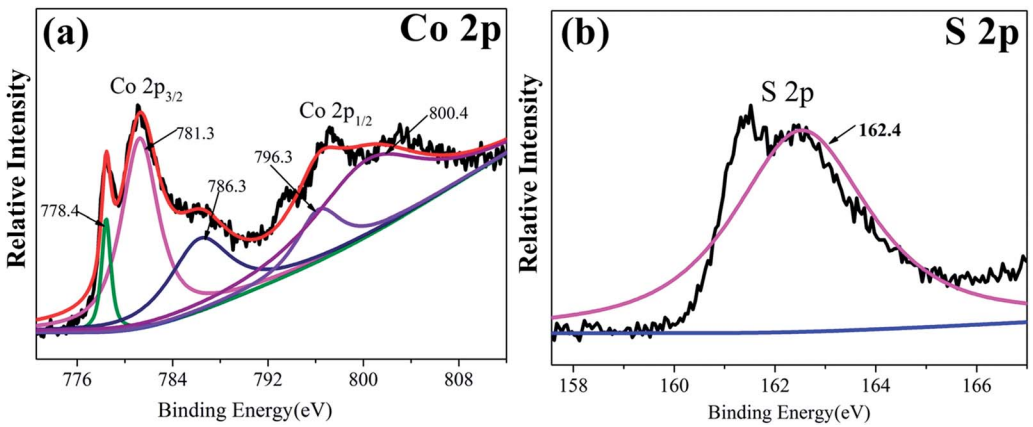

Fig. 3 The XPS spectrum of the Co 2p (a) and S 2p (b). In (a), the peaks at 778.4 eV, 781.3 eV, 786.3 eV, 796.3 eV and 800.4 eV are characteristic of Co^{2+} and Co^{3+}; in (b), the peak at 161.9 eV is the binding energy of Co–S.

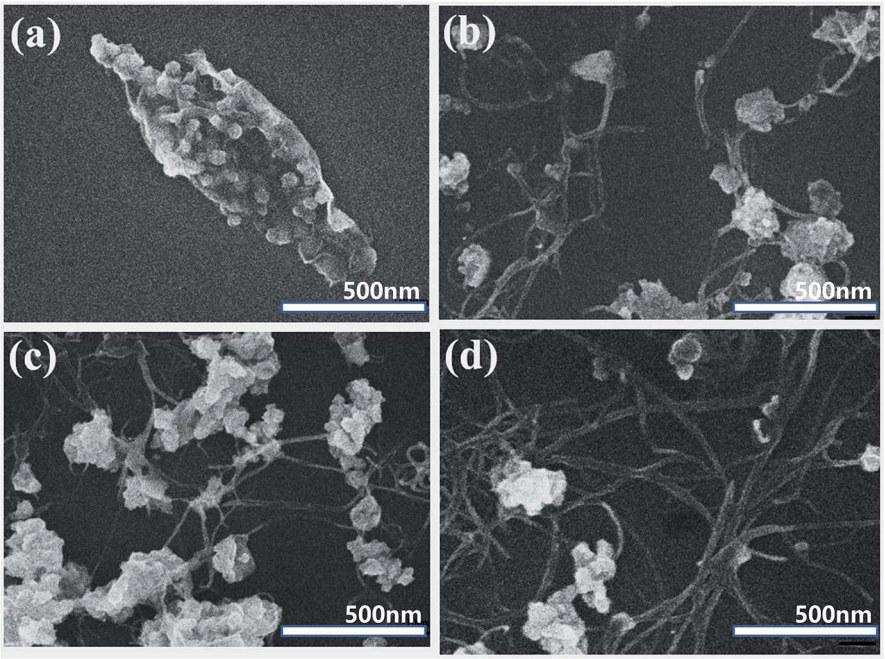

Fig. 4 SEM images of Co_9S_8/RGO (a), Co_9S_8/RGO-10% CNT (b), Co_9S_8/RGO-30% CNT (c) and Co_9S_8/RGO-50% CNT (d). CNT and graphene sheets intertwine and form an interconnected structure.

noteworthy that Co_9S_8/RGO groups are connected to each other by CNTs. The results indicate that with the unique structural properties of RGO and highly conductive nature of uniformly interconnected CNT network, such continuous interconnected network finally can render well-developed porous structures, high mechanical strength, and superior flexibility of the Co_9S_8/RGO-CNT composites, and hence can be considered as an ideal electrode material in supercapacitors.[35,36]

3.2 Electrochemical characterization of Co_9S_8/RGO-CNT

The capacitive properties of the composite materials were assessed by CV, galvanostatic charge–discharge and EIS measurements.

Fig. 6a–d shows the CV curves of pure Co_9S_8/RGO and Co_9S_8/RGO-CNT with the voltage range of −0.1 V to 0.6 V and various scan rates ranging from 5 mV s^{-1} to 50 mV s^{-1}. The CV curves of

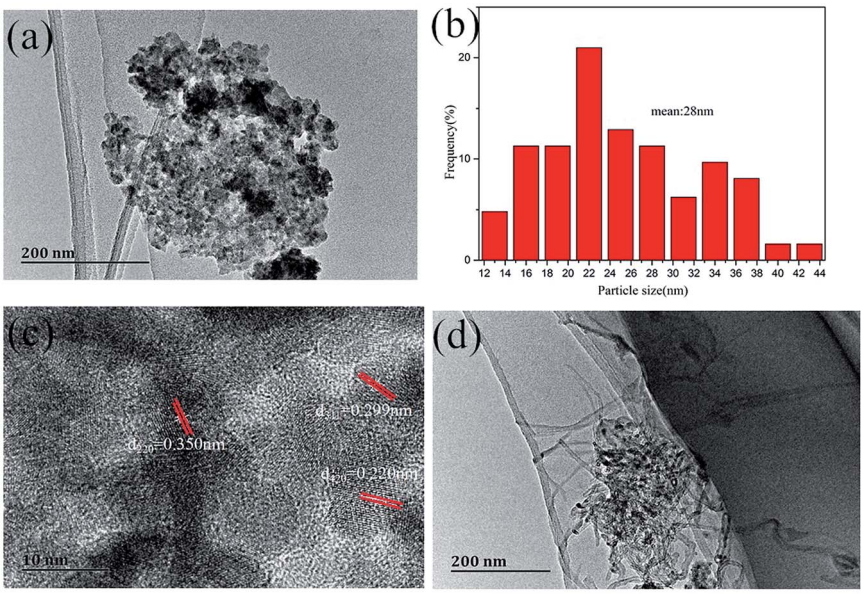

Fig. 5 (a) TEM image of Co_9S_8/RGO, (b) Co_9S_8 nanoparticle distribution diagram, with the average size of Co_9S_8 particles of 28 nm, (c) HR-TEM image of Co_9S_8/RGO, *d*-spacing of 0.350 nm, 299 nm and 0.220 nm correspond to the (220), (311) and (420) planes of Co_9S_8, respectively, and (d) TEM image of Co_9S_8/RGO-CNT.

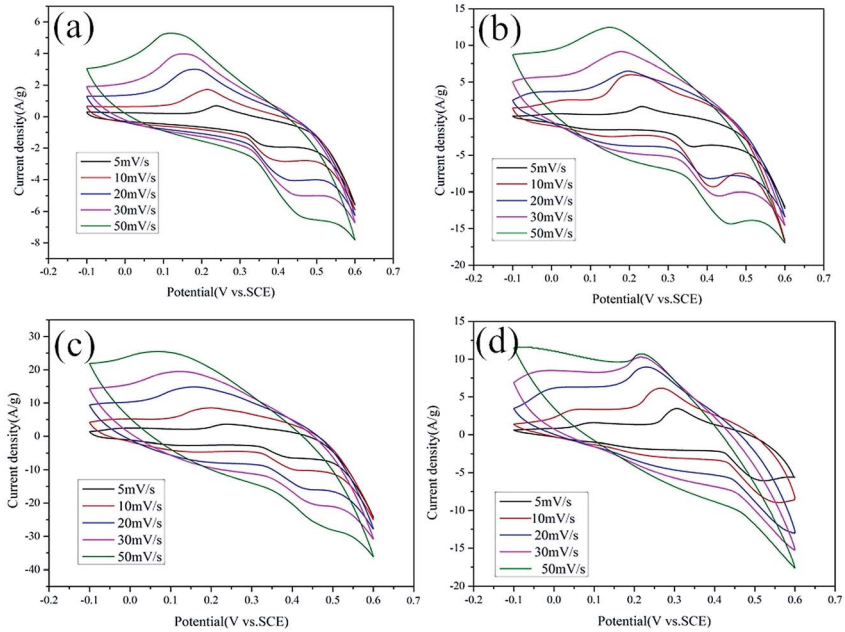

Fig. 6 CV curves of pure RGO (a), Co_9S_8 (b), Co_9S_8/RGO (c) and Co_9S_8/RGO-CNT (d) at different scan rates in a three-electrode system.

Co_9S_8 and Co_9S_8/RGO-CNT have two nearly reversible and symmetrical redox peaks, indicating good capacitive behavior. Though there is no unified conclusion explaining the reaction mechanism of Co_9S_8, it is reported that Co_9S_8 may react with the form between Co^{2+}, Co^{3+} and Co^{4+}, and it can be described as the following reaction:[37]

$$Co_9S_8 + OH^- \rightarrow Co_9S_7OH + e^- \quad (3)$$

$$Co_9S_7OH + OH^- \rightarrow Co_9S_6(OH)_2 + e \quad (4)$$

The specific capacitance of Co_9S_8/RGO was calculated by CV curves using a standard equation as stated in the Experimental section. The highest specific capacitance of RGO, Co_9S_8 and Co_9S_8/RGO was found to be 243.99 F g^{-1}, 541.99 F g^{-1} and 709.25 F g^{-1}, respectively, while that of Co_9S_8/RGO-CNT is

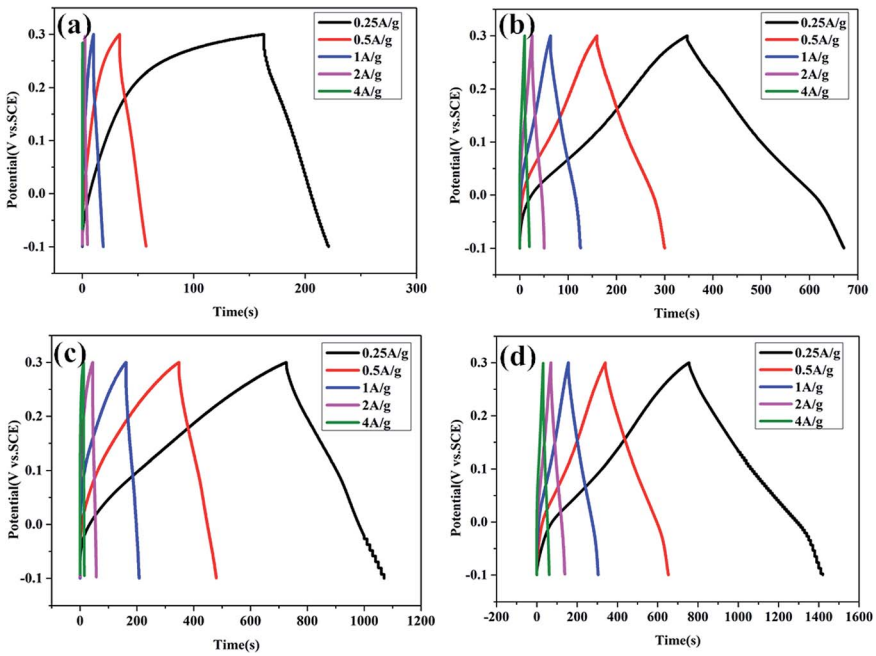

Fig. 7 The galvanostatic charge–discharge curves of pure RGO (a), Co_9S_8 (b), Co_9S_8/RGO (c) and Co_9S_8/RGO-CNT (d) at various current densities in the three-electrode system.

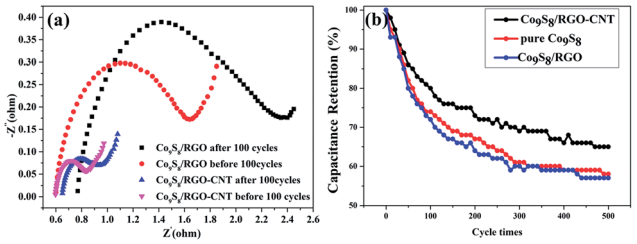

Fig. 8 (a) Nyquist plots before and after 100 cycles for Co_9S_8/RGO and Co_9S_8/RGO-CNT, respectively; the smaller semi-circle and larger slope of Co_9S_8/RGO-CNT shows that adding CNT forms the intertwined structure and improves the conductive performance. (b) The specific capacitance retention curves of Co_9S_8/RGO and Co_9S_8/RGO-CNT.

1376.78 F g^{-1} at scan rate of 5 mV s^{-1}; it was also found to decrease with increasing current density. The reduction of specific capacitance may be attributed to the reduced ion concentration between the electrolyte and electrode interface.

The charge–discharge cycles of Co_9S_8/RGO and Co_9S_8/RGO-CNT are shown in Fig. 7a–d, which were carried out at various current densities between 0.5 A g^{-1} and 4 A g^{-1} and at the voltage range of −0.1 V to 0.3 V in 1 M KOH electrolyte. The charge–discharge curves show a nearly symmetrical and linear shape, presenting good supercapacitive behaviors.

The electrochemical impedance measurements were carried out at the frequency range of 100 kHz to 0.01 Hz, as shown in Fig. 8a. It can be easily observed that the Nyquist plots before and after 100 cycles consist of a semi-circle in the high frequency and a straight line in the low frequency, which is the typical feature of capacitive behavior and characteristic of ion diffusion in the electrode. Comparing the curve of Co_9S_8/RGO with Co_9S_8/RGO-CNT before 100 cycles, the radius of the semicircle of Co_9S_8/RGO-CNT is much smaller than that of Co_9S_8/RGO, which is attributed to the Co_9S_8/RGO-CNT composites' interconnected structure and better conductive performance. At the low-frequency district, the slope of Co_9S_8/RGO is lower than that of Co_9S_8/RGO-CNT, indicating that the interface impedance of Co_9S_8/RGO-CNT is less, which shows its better conductive performance. As for the high-frequency district, the radius of the semicircle represents charge transfer impedance, and the larger the radius, the greater the impedance and the lower the charge transfer.[13,28,29] Therefore, it is concluded that Co_9S_8/RGO-CNT is better than Co_9S_8/RGO.

Long cycling behavior is a major factor for the practical application of supercapacitors, and the values of specific capacitance after 500 cycles are shown in Fig. 8b. From the curves, the specific capacitance retention ratio of Co_9S_8/RGO is 55% after 500 cycles, while the Co_9S_8/RGO with 30% CNT is 65%, which shows better cycling stability.

4 Conclusions

In summary, we have successfully synthesized Co_9S_8/RGO-CNT using hydrothermal and vacuum-filtration methods. SEM and TEM images show that the morphologies of Co_9S_8/RGO-CNT have a unique 3D structure caused by graphene and CNTs interconnected together. Moreover, the excellent electrochemical performance of Co_9S_8/RGO-CNT composites is attributed to the conductive 3D interconnected network composed by interconnected graphene sheets and CNTs, which provide a fast and continuous highway for electron and ion transfer and accommodate the load of Co_9S_8 particles during charge/discharge cycling. The unique structure can guarantee a better specific capacitance as well as charge–discharge and long-term stability, which shows a good prospect for the future. The highest specific capacitance of Co_9S_8/RGO-CNT is 1376.78 F g^{-1} at the scan rate of 5 mV s^{-1}, and the specific capacitance of Co_9S_8/RGO-CNT is 894.9 F g^{-1} after 500 cycles. The outstanding electrochemical properties of Co_9S_8/RGO-CNT suggest that it is a promising electrode material for supercapacitors.

Acknowledgements

The authors of this study gratefully acknowledge Beihang University MSE School for the TEM and SEM. Many thanks also go to Dr Li Ye, Dr Han Xiao and Dr Zhao Xiaoran for their helpful input.

Notes and references

1 X. Li, X. Wang, L. Zhang, S. Lee and H. Dai, *Science*, 2008, **319**, 1229–1232.
2 F. Bonacco, L. Colombo, G. H. Lu, *et al.*, *Science*, 2015, **347**, 1246501–1246509.
3 B. Wang, *J. Mater. Chem.*, 2012, **229**, 15750–15756.
4 G. Q. Zhang, H. B. Wu, H. E. Hoster, M. B. Chan-Park and X. W. Lou, *Energy Environ. Sci.*, 2012, **5**, 9453–9456.
5 X. Y. Dong, L. Wang, D. Wang, C. Li and J. Lin, *Langmuir*, 2012, **28**, 293–298.
6 M. M. Yao, Z. H. Hu, Z. J. Xu and Y. F. Liu, *J. Alloys Compd.*, 2015, **644**, 721–728.
7 L. Huang, D. C. Chen, Y. Ding, S. Feng, Z. L. Wang and M. L. Liu, *Nano Lett.*, 2013, **13**, 3135–3139.
8 M. D. Stoller, S. Murali, N. Quarles, Y. W. Zhu, J. R. Potts, X. J. Zhu, H. W. Ha and R. S. Ruoff, *Phys. Chem. Chem. Phys.*, 2012, **14**, 3388–3391.
9 T. C. Liu, W. G. Pell and B. E. Conway, *Electrochim. Acta*, 1997, **42**, 3541–3552.
10 G. Rajeshkhanna, E. Umeshbabu, P. Justin and G. R. Rao, *Int. J. Hydrogen Energy*, 2015, **40**, 12303–12314.
11 L. Chuan, A. James and N. Branko, *J. Electrochem. Soc.*, 1998, **145**, 4097–4101.
12 J. Cheng, B. Wang, H. L. Xin, *et al.*, *J. Mater. Chem. A*, 2013, **1**, 10814–10820.
13 L. Cao, L. B. Kong, Y. Y. Liang, *et al.*, *Chem. Commun.*, 2004, **14**, 1646–1647.
14 P. Simon and Y. Gogotsi, *Nat. Mater.*, 2008, **7**, 845–854.
15 W. Chen, S. Li, C. Chen and L. Yan, *Adv. Mater.*, 2011, **23**, 5679–5683.
16 M. Pumera, *Energy Environ. Sci.*, 2011, **3**, 668–674.
17 W. Chen and L. Yan, *Nanoscale*, 2011, **3**, 3132–3137.

18 S. Niu, W. Lv, C. Zhang, Y. Shi, J. Zhao, B. Li, Q.-H. Yang and F. Kang, *J. Power Sources*, 2015, **295**, 182–189.
19 X. L. Jia, Z. Chen, X. Cui, Y. T. Peng, X. L. Wang, G. Wang, F. Wei and Y. F. Lu, *ACS Nano*, 2012, **6**, 9911–9919.
20 Y. Wang, Y. P. Wu, Y. Huang, F. Zhang, X. Yang, Y. F. Ma and Y. S. Chen, *J. Phys. Chem. C*, 2011, **115**, 23192–23197.
21 Q. Cheng, J. Tang, J. Ma, H. Zhang, N. Shinya and L. C. Qin, *Phys. Chem. Chem. Phys.*, 2011, **13**, 438–444.
22 N. Jha, P. Ramesh, E. Bekyarova, M. E. Itkis and R. C. Haddon, *Adv. Energy Mater.*, 2012, **2**, 438–444.
23 K. Y. Ma, J. P. Cheng, F. Liu and X. B. Zhang, *J. Alloys Compd.*, 2016, **679**, 277–284.
24 G. X. Wang, J. Yang, J. Park, X. L. Gou, B. Wang, H. Liu and J. Yao, *J. Phys. Chem. C*, 2008, **112**, 8192–8195.
25 M. C. Liu, Y. Zhao, S. Gao, Y. Wang, Y. X. Duan, X. Han and Q. Dong, *New J. Chem.*, 2015, **39**, 1094–1100.
26 H. Jiang, C. Z. Li, T. Sun and J. Ma, *Nanoscale*, 2012, **4**, 807–812.
27 C. H. Zheng, T. Yao, *et al.*, *J. Alloys Compd.*, 2016, **678**, 93–101.
28 J. Pu, Z. H. Wang, K. L. Wu, N. Yu and E. H. Sheng, *Phys. Chem. Chem. Phys.*, 2014, **16**, 785–791.
29 R. B. Rakhi, N. A. Alhebshi, D. H. Anjum and H. N. Alshareef, *J. Mater. Chem. A*, 2014, **2**, 16190–16198.
30 J. F. Li, S. L. Xiong, Y. R. Liu, Z. C. Ju and Y. Qian, *ACS Appl. Mater. Interfaces*, 2013, **5**, 981–988.
31 P. F. Yin, L. L. Sun, Y. L. Gao and S. Y. Wang, *Bull. Mater. Sci.*, 2008, **31**, 593–596.
32 R. Ramachandram, M. Saranya, C. Santhosh, V. Velmurugan, B. P. C. Raghupathy, S. K. Jeong and A. N. Grace, *RSC Adv.*, 2014, 421151–451162.
33 S. J. Bao, Y. B. Li, C. M. Li, Q. L. Bao, Q. Lu and J. Guo, *Cryst. Growth Des.*, 2008, 83745–83749.
34 S. Peng, L. Li, X. Han, W. Sun and M. Srinivasan, *Angew. Chem., Int. Ed.*, 2014, **53**, 12594–12599.
35 F. Fu, Y. Chen, P. Li, J. He, Z. Wang, W. Lin and W. Zhang, *RSC Adv.*, 2015, **5**, 71790–71795.
36 M. Zhou, T. Tian, X. Li, X. Sun, J. Zhang, Y. Chen, P. Cui, J. Tang and L. C. Qin, *Chem. Phys. Lett.*, 2013, **581**, 64–69.
37 X. Zhang, D. Zhao, P. Tang, Y. Shen, C. Xu, H. Lia and Y. Xiao, *J. Mater. Chem. A*, 2013, **1**, 3706–3712.